Supporting Information

Ultra-Sensitive Flow Sensing of a Single Cell Using Graphene-based Optical Sensors

Fei Xing,[1] Gui-Xian Meng,[1] Qian Zhang,[2] Lei-Ting Pan,[1] Peng Wang,[1] Zhi-Bo Liu,[1] Wen-Shuai Jiang,[1] Yongsheng Chen,[2] and Jian-Guo Tian[1]

[1] The Key Laboratory of Weak Light Nonlinear Photonics, Ministry of Education, Teda Applied Physics School and School of Physics, Nankai University, Tianjin 300457, China

[2] The Key Laboratory of Functional Polymer Materials and Center for Nanoscale Science & Technology, Institute of Polymer Chemistry, College of Chemistry, Nankai University, Tianjin 300071, China

1) Materials and methods

Preparation of GO. GO is prepared from natural graphite by the modified Hummer's method, which is employed as the starting material in the fabrication of a high-quality graphene film.

Fabrication of rGO films. Quartz slides were cleaned in an ultrasonic bath with detergent, deionized water, acetone, and isopropyl alcohol. The slides were rinsed thoroughly with deionized water, dried under a nitrogen stream, and stored in a vacuum oven at 80°C until use, which typically occurred within 2 h. The pre-cleaned quartz was treated with ozone for 2 min prior to use. Subsequently, a GO dispersion in water was spin-coated on its surface, and the GO film on the quartz was thermally annealed at a high temperature.

Preparation of a microfluidic chip. Poly(dimethylsiloxane) (PDMS) is biocompatible and chemically stable. Thus, it is a suitable material for the fabrication of a microfluidic chip. Computer-aided design (CAD) software programs were employed to design a pattern. The photoresist mask was etched with electron beam lithography. A negative photoresist (SU-8) was spin-coated to the Si base at a speed of 1,100 r/min for 50 s and dried at 110°C. The photoresist mask on the negative photoresist (SU-8) was covered with Si layers and exposed to ultraviolet light; photographic films were developed to obtain the master. A balance was used to weigh 70 g of Sylgard 184 silicone elastomer base and 7 g

of Sylgard 184 elastomer curing agent (10:1 ratio). After the base and curing agent were completely mixed, the liquid mixture was placed into the vacuum line of the fume hood to trap any bubbles for 1 h. The liquid mixture was poured on the master, and the dish containing both the master and PDMS prepolymer was placed in an oven set to 70°C and cured for 3 h. The solidified PDMS microfluidic chip was then peeled off the master with pliers.

Preparation of the GSOCS. The previously prepared *h*-rGO films/quartz structure and PDMS microfluidic chip were processed in plasma oxygen by cleaning them with 150 W of power for 30 s. The irreversible h-rGO films/quartz structure was adhered to a PDMS microfluidic chip to obtain the GSOCS with a microfluidic chip.

Cell extraction and culture. The cells used in the experiments consisted of lymphocytes and Jurkat cells. Lymphocytes were obtained from the blood of normal healthy adults, whereas the Jurkat cells, which comprise an immortalized line of human T lymphocyte cells, were obtained from Prof. Li Junying's laboratory. The cells were grown in a RPMI 1640 medium (10.4 g/L RPMI 1640, 2 g/L NaHCO3, 5.96 g/L HEPES, 0.05 g/L penicillin G, 0.1 g/L streptomycin sulfate, pH 7.2) and cultured at 37°C in a MCO175 incubator (SANYO Electric Biomedical Co., Ltd., Osaka, Japan) that contained 5% CO_2. The cells were suspended in HBSS (145 mM NaCl, 5 mM KCl, 1 mM $CaCl_2$, 1 mM $MgCl_2$, 10 mM HEPES, and 10 mM glucose, PH 7.4) at 6×105 cells/cm2 and retained in an ice bath prior to use.

2) The resolution and sensitivity of RI sensing, under θ_c= 67.6° conditions.

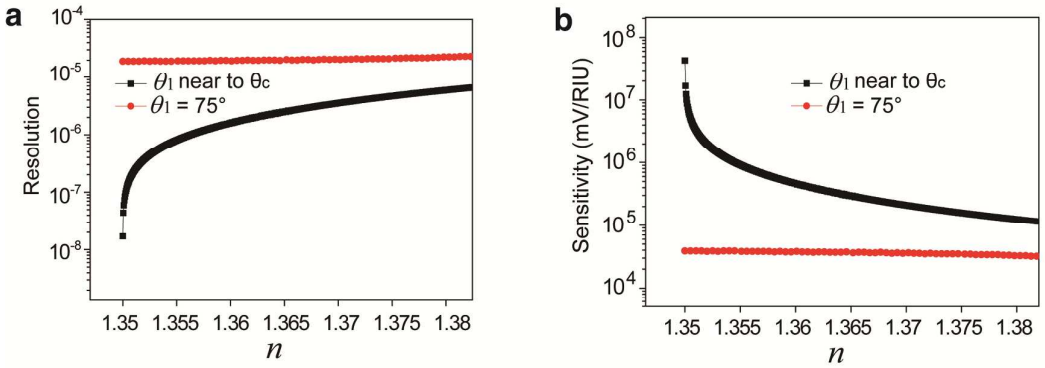

Figure S1. The RI-dependent resolution and sensitivity plots of the *h*-rGO enhanced RI sensor. Fixed the incidence angle θ_1 equals to the critical angle θ_c= 67.6°, which occurs at the interface between the medium 2 (n_2= 1.35) and the quartz (n_{quartz} = 1.47).

Since 1.35 is the critical refractive index in the experiments of single cell measurement, the TIR will be formed when medium 2 is greater than 1.35. The refractive index of the measurement target cells are generally greater than 1.35, so we use 1.35 to simulate.

Once the medim 2 appears cells or microspheres (refractive index greater than 1.35), total internal reflection occurs. Medium 2 represents the cells or microspheres across the detection window. The thickness of the *h*-rGO is 8.1 nm, and its optical constant is $\hat{n} = 2.6 + 1.25i$. The α is 0.00361 μW/mV, and the V_n is ~10 mV. Under these conditions, the RI-dependent resolution and sensitivity plots of the *h*-rGO enhanced RI sensor are shown in the black line symbol plots of Figure S1. The limit resolution and sensitivity of the *h*-rGO enhanced RI sensing are almost the same as these in the main text respectively. The results show that the ultrahigh resolution and sensitivity of RI sensing can be adjusted to any RI range by adjusting incidence angle θ_1.

3) The characterization of *h*-rGO.

Table S1 shows the specific parameters of fewer layers *h*-rGO preparation. Figure S2 shows the AFM images of different thickness of *h*-rGO. The type of detection is tapping mode and scan rate is 1.003 Hz. The resonant frequency and force constant of cantilever are 300 kHz and 40 N/m. We can see from the images, by varying the concentrations of graphene oxide (GO) and speeds of spin-coating, the thickness of the *h*-rGO can be controlled accurately in the range of a few nanometers. Figure S3 shows the raman spectroscopy of few layers of *h*-rGO. The wavelength of laser source to achieve Raman signal is 514 nm and the exposure time is 10 s. It exhibits the characteristic D and G peaks of graphene materials. The characteristic graphene D and G bands at 1354 and 1596 cm^{-1}.

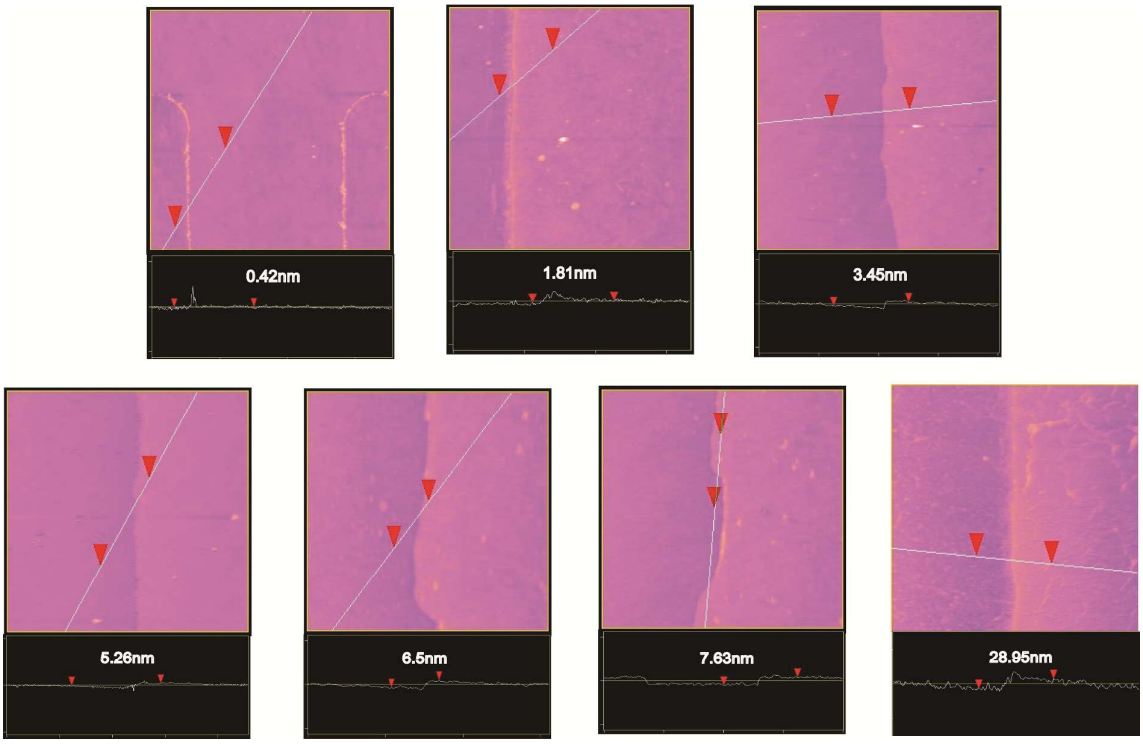

Figure S2. The AFM images of different thickness of *h*-rGO.

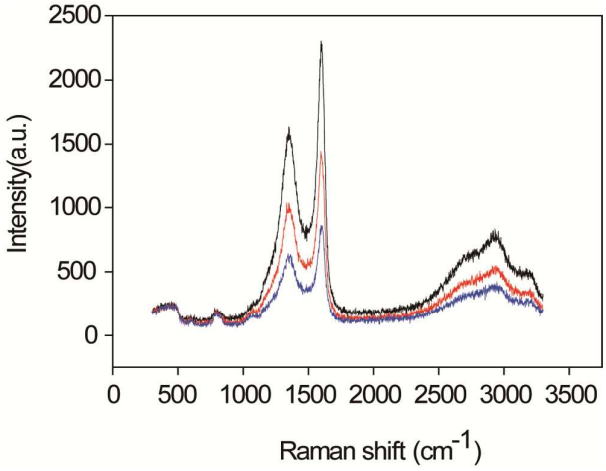

Figure S3. The raman spectroscopy of few layers of *h*-rGO.

4) The simulation results of the optimal thickness of CVD graphene for RI sensing.

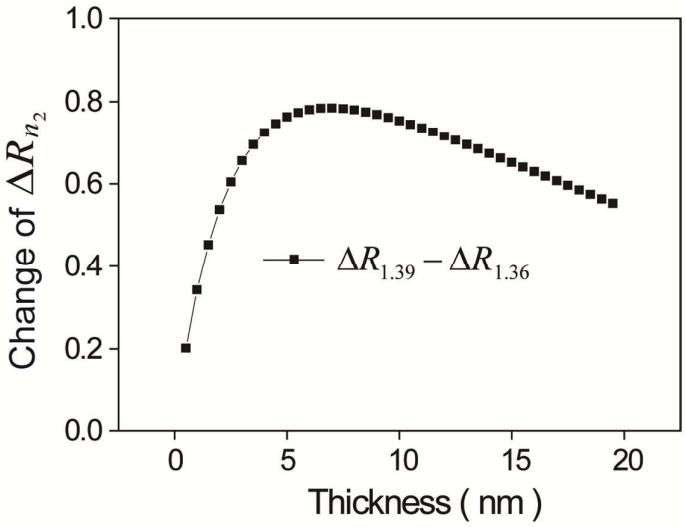

Figure S4. The simulation result of the optimal thickness of CVD graphene.

To achieve the most sensitive sensing needs, it can be concluded that the optimal thickness of graphene is ~ 20 layers (Figure S4), with the standard optical constants of graphene ($\hat{n} = 2.6 + 1.3i$) by calculation.

5) The comparison of surface roughness.

Compared with ~20 layers CVD graphene, the whole surface of 8.13 nm *h*-rGO is uniform. It can be seen that residual (the red circle) and fold (the blue circle) are on the surface of ~20 layers CVD graphene in Figure S5. The surface roughness of 8.13 nm *h*-rGO is 2.5 nm and the surface roughness of ~20 layers CVD graphene is 16.7 nm inside the black box.

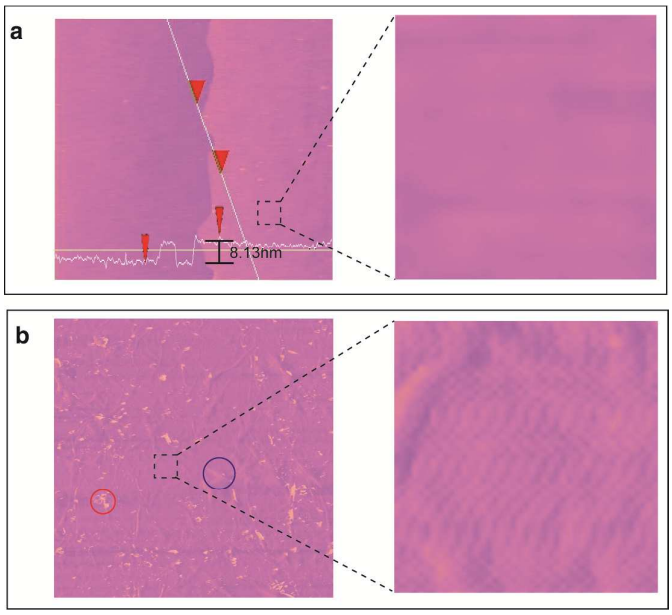

Figure S5. The AFM images of 8.13 nm h-rGO and ~20 layers CVD graphene. **a**. The surface roughness analysis of 8.13 nm h-rGO. **b**. The surface roughness analysis of ~20 layers CVD graphene.

6) The comparison of anti-shedding performance.

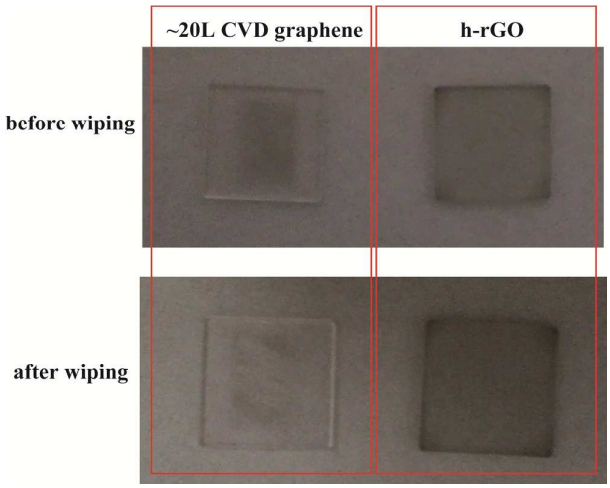

Figure S6. The comparison of anti-shedding performance between 8.13 nm h-rGO and ~20 layers CVD graphene.

Compared with ~20 layers CVD graphene, it is difficult to exfoliate h-rGO from the substrate by using a cotton swab.

7) The absorption effect of polarization of *h*-rGO, CVD graphene and GO.

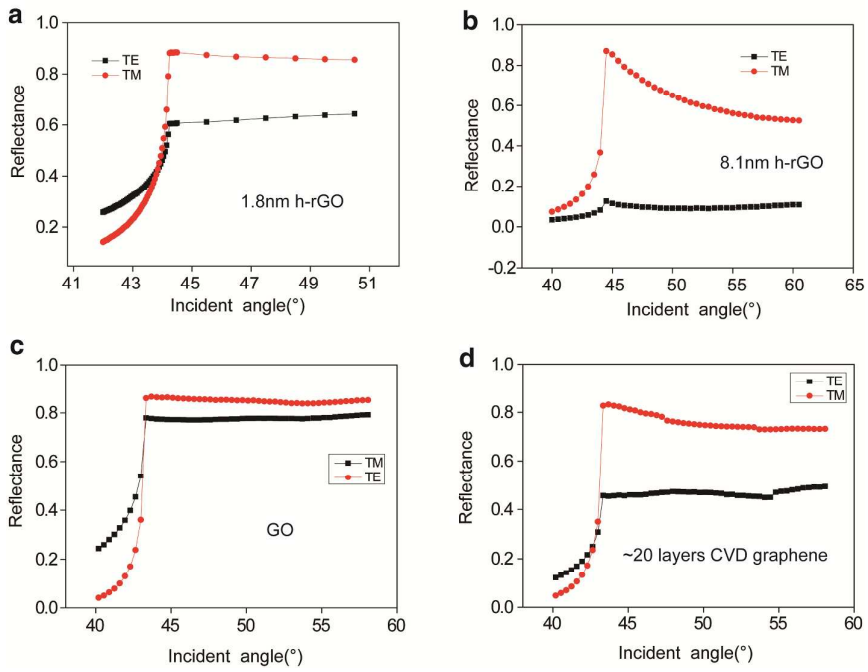

Figure S7. The reflectance plots of TE and TM modes. **a**. The reflectance plots of 1.8 nm *h*-rGO. **b**. The reflectance plots of 8.1 nm *h*-rGO. **c**. The reflectance plots of ~8 nm GO. **d**. The reflectance plots of ~20 layers CVD graphene.

The reflectance plots of TE and TM modes, under different thickness of *h*-rGO conditions, are shown in Figure S7a and b. As mentioned in the main text, the *h*-rGO films have large absorption effect of polarization. As shown in Figure S7a and d, , the absorption effect of polarization of few layer *h*-rGO is equally large as CVD graphene. Meanwhile, when the thickness of *h*-rGO is 8.1 nm, there is a large absorption effect of polarization. And reflectance difference of TE and TM modes can be changed from ~5% to ~90% in a range of incidence angle. The calculating results in the main text show the best fitting optical constant $\hat{n}$ of *h*-rGO films is obtained with $\hat{n} = 2.6 + 1.25i$, Where, 2.6 and 1.25 represent the real refractive index and extinction coefficient of *h*-rGO films, respectively. The extinction coefficient of *h*-rGO is smaller than that of mechanically exfoliated graphene reported. This result suggests that under the same polarization absorption conditions, *h*-rGO films has a higher transmittance than mechanically exfoliated graphene. And when the reduction temperature is low (600°C), the extinction coefficient of *h*-rGO films is ~1, which is significantly lower than mechanically exfoliated graphene. The parameters of fewer layers of h-rGO shown in Table S1. The reflectance plots of ~8 nm GO (Figure S7c) shows weak absorption effect of polarization. Figure S7d shows the reflectance plots of ~20 layers CVD graphene.

Table S1. The parameters of fewer layers *h*-rGO preparation.

Thickness (nm)	Optical constants ($\hat{n} = n + \kappa i$)	Concentration of GO (mg/mL)	Speed of spin-coating (r/min)	Temperature (℃)
8.13	$\hat{n} = 2.6 + 1.25i$	5	2000	950
7.63	$\hat{n} = 2.6 + 1.26i$	5	3000	950
6.5	$\hat{n} = 2.6 + 1.25i$	4	2000	950
5.26	$\hat{n} = 2.6 + 1i$	4	3000	950
3.45	$\hat{n} = 2.6 + 1.25i$	3	2000	950
2.07	$\hat{n} = 2.6 + 1i$	2	2000	600
1.8	$\hat{n} = 2.6 + 1.18i$	2	3000	600
0.42	$\hat{n} = 2.6 + 1i$	1	3000	600

8) The FWHM statistical results of 6 μm PS microspheres detected by the GSOCS.

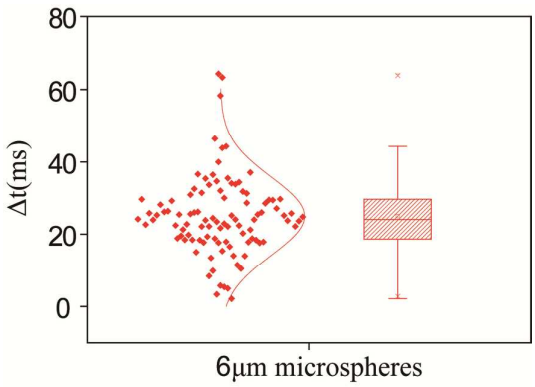

Figure S8. The FWHM statistical results of 6 μm PS microspheres detected by the GSOCS. The flow rate is 3 μl/hour.

9) The statistical results of T lumphocytes and jurkat cells detected by the commercial FCM.

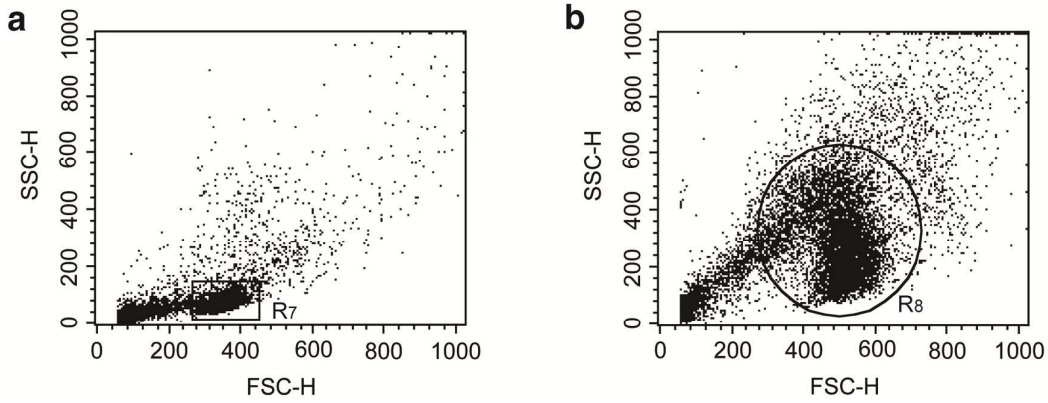

Figure S9. The statistical charts of T lumphocytes and jurkat cells detected by the commercial FCM, respectively.

10) The multilayer structure model and transfer-matrix method for calculations

To calculate the reflectance of the TE and TM polarized light, a multilayer structure model with the transfer-matrix method was developed in our previous work[1,2]. For Figure 1, we used the trilayer structure (SiO_2 ($n_1 = 1.47$, semi-infinite) / h-rGO ($\hat{n}$, thickness d)/ low-index medium (n_2 , semi-infinite)). The reflectance (R_{TE} , R_{TM}) at the incident angle θ_I

can be got once given $\hat{n}$, d and n_2, afterwards the reflectance ratio (R_{TM}/R_{TE}) and reflectance difference (ΔR) can also be achieved.

In details, in Figure 1b it is a plot of reflectance ratio as a function of incident angle, where $n_2 = 1$(air), $\hat{n}$ and d of h-rGO are given in Tabel S1; In Figure 1c, the plots are changes of ΔR at different n_2 as a function of d (from 0 to 20 nm), the incident angle was fixed to 65°, $n_2 = 1.33, 1.36\ 1.39$, $\hat{n} = 2.6 + 1.25i$; In Figure 1e, the two incident angles are choised to be 65° (near θ_C) and 75°, respectively. n_2 varies from 1.33 to 1.36, $\hat{n} = 2.6 + 1.25i$, and $d = 8.1$ nm (the optimum thickness). Firstly, we can have reflectance difference (ΔR) as a function of n_2, and then the sensitivity and resolution can be deduced using Equations (1) and (2), in which α is the response of the balanced detector, P_0 is the power of TE or TM mode, V_n is the noise value.

As shown below, for a general multilayer structure the reflectance calculations can be deduced based on Maxwell equations [1,2], and the trilayer structure is a specific one.

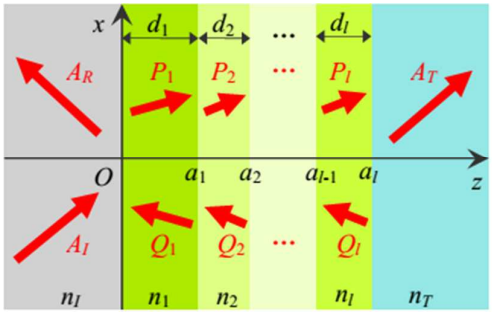

Figure S10. Schematics of multilayered structure

A general multilayered structure is shown in Figure S10. The incidence plane of light is assumed to be x, z-plane. The structure consists of l ($l \geqslant 0$) slabs sandwiched between two semi-infinite spaces. The thickness and refractive indices of ith slab are given by $d_i (i = 1, 2, ...l)$ and $n_i = (\varepsilon_i \mu_i)^{\frac{1}{2}} (i = 1, 2, ...l)$, where ε_i and μ_i are relative permittivity and relative permeability of the ith slab. The refractive indices of incident and exit spaces are given by $n_I = (\varepsilon_I \mu_I)^{\frac{1}{2}}$ and $n_T = (\varepsilon_T \mu_T)^{\frac{1}{2}}$, respectively. And the boundaries are given by $a_i (i = 0, 1, 2, ..., l)$,where $a_0 = 0$.

In each layer, the electromagnetic fields of light can be expressed as superpositions positive- and negative-going components. The fields of E and H can be obtained by solving the vector wave equation under constraint of tangential field continuity. Uniqueness of the

solutions is guaranteed by the Helmholtz theorem. For TE polarization, the field components are written as follows:

$$\begin{cases} H_x = \dfrac{-k_{Iz}}{\omega\mu_0\mu_I}(A_I e^{ik_{Iz}z} - A_R e^{-ik_{Iz}z})e^{ik_x x}, \\ E_y = (A_I e^{ik_{Iz}z} + A_R e^{-ik_{Iz}z})e^{ik_x x}, \qquad (z < a_0 = 0) \\ H_z = \dfrac{k_x}{\omega\mu_0\mu_I}(A_I e^{ik_{Iz}z} + A_R e^{-ik_{Iz}z})e^{ik_x x}, \end{cases} \tag{1}$$

$$\begin{cases} H_x = \dfrac{-k_{iz}}{\omega\mu_0\mu_i}(P_i e^{ik_{iz}(z-a_{i-1})} - Q_i e^{-ik_{iz}(z-a_i)})e^{ik_x x}, \\ E_y = (P_i e^{ik_{iz}(z-a_{i-1})} + Q_i e^{-ik_{iz}(z-a_i)})e^{ik_x x}, \qquad (a_{i-1} < z < a_i (i = 1,2,...,l)) \\ H_z = \dfrac{k_x}{\omega\mu_0\mu_i}(P_i e^{ik_{iz}(z-a_{i-1})} + Q_i e^{-ik_{iz}(z-a_i)})e^{ik_x x}, \end{cases} \tag{2}$$

$$\begin{cases} H_x = \dfrac{-k_{Tz}}{\omega\mu_0\mu_T} A_T e^{ik_{Tz}(z-a_l)} e^{ik_x x}, \\ E_y = A_T e^{ik_{Tz}(z-a_l)} e^{ik_x x}, \qquad (z > a_l) \\ H_z = \dfrac{k_x}{\omega\mu_0\mu_T} A_T e^{ik_{Tz}(z-a_l)} e^{ik_x x}, \end{cases} \tag{3}$$

where, $k_{Iz} = (n_I{}^2 k_0{}^2 - k_x{}^2)^{\frac{1}{2}}$, $k_{iz} = (n_i{}^2 k_0{}^2 - k_x{}^2)^{\frac{1}{2}} (i = 1,2,...,l)$, $k_{Tz} = (n_T{}^2 k_0{}^2 - k_x{}^2)^{\frac{1}{2}}$, $k_0 = 2\pi / \lambda_0$ is the vacuum wave vector and λ_0 is the free space wavelength, $k_x = k_0 \sin(\theta)$ (θ is the incident angle). The amplitude coefficients can be deduced according to the boundary condition of continuities of Hx and Ey. The relation between the amplitude coefficients are given by

$$\begin{bmatrix} A_I \\ A_R \end{bmatrix} = \mathbf{M_0} \begin{bmatrix} P_1 \\ Q_1 \end{bmatrix}, \quad \begin{bmatrix} P_i \\ Q_i \end{bmatrix} = \mathbf{M_i} \begin{bmatrix} P_{i+1} \\ Q_{i+1} \end{bmatrix}, \quad \begin{bmatrix} P_l \\ Q_l \end{bmatrix} = \mathbf{M_l} A_T, \tag{4}$$

where,

$$\mathbf{M_0} = \frac{1}{2}\begin{bmatrix} 1+K_{1I} & (1-K_{1I})e^{ik_{1z}d_1} \\ 1-K_{1I} & (1+K_{1I})e^{ik_{1z}d_1} \end{bmatrix}, \tag{5}$$

$$\mathbf{M}_i = \frac{1}{2} \times \begin{bmatrix} 1+K_{i+1,i}e^{-ik_{iz}d_i} & (1-K_{i+1,i})e^{ik_{i+1,z}d_{i+1}}e^{-ik_{iz}d_i} \\ 1-K_{i+1,i} & (1+K_{i+1,i})e^{ik_{i+1,z}d_{i+1}} \end{bmatrix} \tag{6}$$

$$\mathbf{M_l} = \frac{1}{2}\begin{bmatrix} (1+K_{Tl})e^{-ik_{lz}d_l} \\ 1-K_{Tl} \end{bmatrix}, \tag{7}$$

$$K_{1I} = \frac{k_{1z}}{k_{Iz}}\Gamma_{I1}, \quad K_{i+1,i} = \frac{k_{i+1,z}}{k_{iz}}\Gamma_{i,i+1} \ (i = 1,2,...,l-1), \quad K_{Tl} = \frac{k_{Tz}}{k_{lz}}\Gamma_{lT}, \tag{8}$$

$$\Gamma_{I1} = \frac{\mu_I}{\mu_1}, \qquad \Gamma_{i,i+1} = \frac{\mu_i}{\mu_{i+1}} \ (i = 1,2,...,l-1), \qquad \Gamma_{lT} = \frac{\mu_l}{\mu_T}。 \tag{9}$$

Thus the relation between incident, reflected, and transmitted amplitudes is given by:

$\begin{bmatrix} A_I \\ A_R \end{bmatrix} = \mathbf{M}A_T = \begin{bmatrix} \mathrm{M}_1 \\ \mathrm{M}_2 \end{bmatrix} A_T$ （$\mathbf{M}$ is a 2×1 matrix and is defined by $\mathbf{M} = \prod_{i=0}^{l} \mathbf{M}_i$）.

The light intensity is given by the amplitude of Poynting vector

$$S = |\mathbf{E}\times\mathbf{H}| = \sqrt{\varepsilon/\mu}E^2 = \sqrt{\mu/\varepsilon}H^2 \tag{10}$$

For TE waves, the amount of energy that is incident on a unit area of the boundary ($z=0$) per second is given by

$$J_{\mathrm{I}} = S_{\mathrm{Iz}} = \sqrt{\frac{\varepsilon_0\varepsilon_{\mathrm{I}}}{\mu_0\mu_{\mathrm{I}}}}\frac{k_{\mathrm{Iz}}}{n_1 k_0}|A_{\mathrm{I}}|^2, \tag{11}$$

Similarly, the energies that are reflected and transmitted from unit areas of the boundaries ($z=0$ and $z=d$) per second are given by

$$J_R = S_{Rz} = \sqrt{\frac{\varepsilon_0\varepsilon_I}{\mu_0\mu_I}}\frac{k_{Iz}}{n_I k_0}|A_R|^2, \tag{12}$$

$$J_T = S_{Tz} = \sqrt{\frac{\varepsilon_0\varepsilon_T}{\mu_0\mu_T}}\frac{\mathrm{Re}(k_{Tz})}{n_T k_0}|A_T|^2 . \tag{13}$$

Therefore, the reflectance and transmittance are given by

$$\begin{cases} R = \dfrac{J_R}{J_I} = \left|\dfrac{A_R}{A_I}\right|^2 = \dfrac{M_2 M_2^*}{M_1 M_1^*}, \\ T = \dfrac{J_T}{J_I} = \dfrac{\mu_I}{\mu_T}\dfrac{real(k_{Tz})}{k_{Iz}}\left|\dfrac{A_T}{A_I}\right| = \dfrac{\mu_I}{\mu_T}\dfrac{real(k_{tz})}{k_{Iz}}\dfrac{1}{M_1 M_1^*}, \end{cases} \tag{14}$$

For TM polarized light, owing to the symmetry of Maxwell equations for TE and TM waves, the electromagnetic field distributions can be immediately obtained if one changes E, H, $-\mu$ to H, E, ε, respectively, keeping all the subscripts unchanged. Finally, the reflectance and transmittance for TM polarization can be achieved

$$\begin{cases} R = \dfrac{J_R}{J_I} = \left|\dfrac{A_R}{A_I}\right|^2 = \dfrac{M_2 M_2^*}{M_1 M_1^*}, \\ T = \dfrac{J_T}{J_I} = \dfrac{\varepsilon_I}{\varepsilon_T}\dfrac{real(k_{Tz})}{k_{Iz}}\left|\dfrac{A_T}{A_I}\right| = \dfrac{\varepsilon_I}{\varepsilon_T}\dfrac{real(k_{tz})}{k_{Iz}}\dfrac{1}{M_1 M_1^*}, \end{cases} \tag{15}$$

11) Theoretical model for calculating the flowing sensing of PS microspheres.

In part 10, we have developed the general multilayer structure model to calculate reflectance, in which all the conditions are ideal (infinite in two dimensions and plane waves). In our experiments, the rolling of PS microspheres in the channel can also be regarded as a

dynamic four-layer structure model (Figure S11).

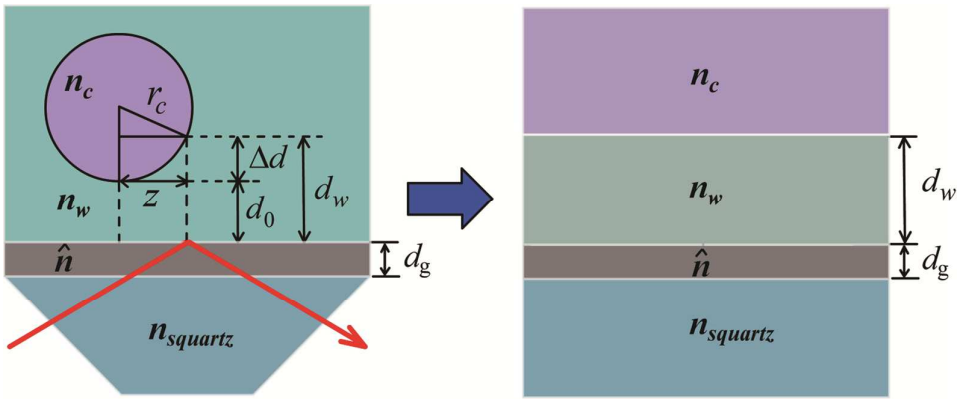

Figure S11. Schematics of an equivalent dynamic four-layer structure model to simulate rolling of PS microspheres across the detection window

In details, the prism/quartz can be regarded as a semi-infinite medium with the refractive index of n_{quartz}=1.47, on the top of the quartz is the *h*-rGO film with the optimum thickness ($\hat{n} = 2.6 + 1.25i$, $d_g = 8.1nm$), in terms of the PS microsphere (or cells) since its radius is far from the wavelength, it can also be regarded as a semi-infinite medium with the refractive index of n_{cell}=1.36. Between the beads and the *h*-rGO film is a water layer with the thickness of d_{water}, as the beads roll across the detection window d_{water} changes as a function of z and d_0 ($d_w = d_0 + \Delta d = d_0 + r_c - \sqrt{r_c^2 - z^2}$).

Applying the developed multilayer structure in part 10 to this dynamic four-layer structure we can simulate the signal (ΔR or sensitivity) of PS microspheres flowing detection (Figure 2c and 2d).

REFERENCES

(1) Ye, Q.; Wang, J.; Liu, Z.; Deng, Z.; Kong, X.; Xing, F.; Chen, X.; Zhou, W.; Zhang, C.; Tian, J. *Appl. Phys. Lett.* **2013**, *102*, 021912.

(2) Xing, F.; Liu, Z.; Deng, Z.; Kong, X.; Yan, X.; Chen, X.; Ye, Q.; Zhang, C.; Chen, Y.; Tian, J. *Scientific Reports* **2012**, *2*, 908.